Section 4

Parameterization of atmospheric and surface processes, effects of different physical parameterizations.

Effect of Cloud Microphysics Scheme and Ice Nuclei on Forecasts for the September 2015 Heavy Rainfall Event in Kanto and Tohoku Regions

Kentaro Araki[1]

1: Meteorological Research Institute, Tsukuba, Ibaraki, Japan

e-mail: araki@mri-jma.go.jp

1. Introduction

Extreme rainfall occurred in the Kanto and Tohoku regions of Japan in September 2015, and flooding and landslides associated with the rainfall killed 8 people. The rainfall amount reached 600 mm in the nourthern Kanto (Fig. 1). The heavy rainfall in Kanto was produced by linear convective systems from 9 to 10 September under the atmospheric condition with a moist southerly airflow associated with an extratropical cyclone over the Japan Sea and southeasterly airflow from Typhoon Kilo (Fig. 2a). A moist easterly airflow also formed linear convective systems and caused the heavy rainfall in Tohoku from 10 to 11 September (Fig. 2b). The operational mesoscale model (MSM) of Japan Meteorological Agency (JMA) successfully forecasted the occurrence of the heavy rainfall events, but a quantitative forecast of rainfall amount remains challenges. Although the aerosols indirect effect has been known to be important in not only the global warming but also mesoscale convective systems, it is not known how the aerosols indirect effect especially by ice nuclei affects precipitation amounts and the atmospheric conditions. For heavy snowfall events in Kanto, it is indicated that aerosols indirect effect by ice nuclei and cloud microphysics schemes considerably affected snowfall amounts and distribution (Araki and Murakami, 2015; Araki, 2016). In this study, we investigated the effects of cloud microphysics schemes and aerosols indirect effect by ice nuclei on the forecast for the rainfall and the atmospheric condition in the September 2015 heavy rainfall event in Kanto and Tohoku regions.

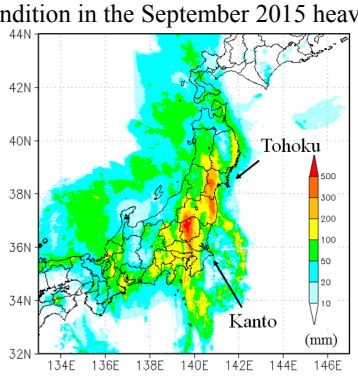

Figure 1. Precipitation amount derived from JMA radar analysis accumulated from 18 UTC on 8 to 00 UTC on 11 September 2015.

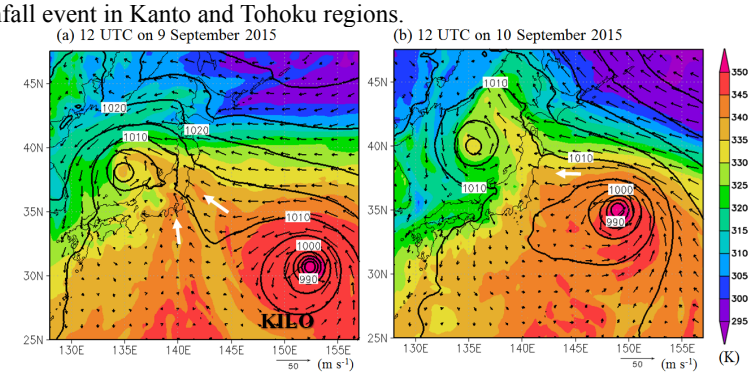

Figure 2. Synoptic conditions derived from the JMA global analysis at (a) 12 UTC on 9 and (b) 12 UTC on 10 September 2015. Shade and contour line indicate equivalent potential temperature (K) at 950 hPa and sea level pressure (hPa), respectively. Vectors show horizontal wind at 950 hPa.

2. Model settings of sensitivity experiments

Numerical simulations were performed by the JMA Non-Hydrostatic Model (NHM) with a domain of 7,000x7,000 km covering Japan and a horizontal grid spacing of 5 km. The initial and boundary conditions were provided from the JRA-55 reanalysis data and the models were run from 18 UTC on 8 to 06 UTC on 11 September 2015. A bulk cloud microphysics scheme with 2-moment cloud ice, snow, and graupel was used in a control run (CNTL). As sensitivity experiments on cloud microphysics schemes, we performed two numerical experiments with a bulk cloud microphysics scheme with 2-moment cloud ice and 1-moment snow and graupel (Ice-2m), and with 1-moment cloud ice, snow, graupel (Ice-1m). Another experiment with the Kain-Fritsch convection parameterization and the cloud microphysics scheme same as CNTL (KF) was also performed. Focusing on the aerosol indirect effect by ice nuclei, two experiments with changing coefficients in the formulas of deposition/condensation-freezing-mode ice nucleation (Meyers, 1992) and immersion-freezing-mode ice nucleation (Bigg, 1955) by factors of 0.1 (IN01) and 10 (IN10) were performed. The other setups in each experiment were the same as those used in the MSM.

3. Effect on rainfall and atmospheric condition

The results of forecasted precipitation in CNTL and the differences from CNTL for each experiment are shown in Fig. 3. Although the CNTL somewhat overestimated the precipitation amount especially in the northern Japan including Tohoku compared with the observation, the heavy rainfalls in Kanto and Tohoku regions were successfully reproduced. In each sensitivity experiment, there were the difference of heavy rainfall areas with precipitation amount over 100 mm from CNTL because the differences of the representation for the location, duration time, and precipitation intensity of linear convective systems. In Tohoku, precipitation amount increased in the coastal areas and decreased inland areas in both KF and IN01 compared with the CNTL, and opposite features were found in Ice-2m, Ice-1m, and IN01. To examine the atmospheric conditions causing the differences in precipitation between these experiments, equivalent potential temperature (EPT) fields at 950 hPa were investigated (Fig. 4). It is found that there were positive (negative) differences of EPT on the windward side of the Tohoku in KF and IN01 (Ice-2m, Ice-1m, and IN01) from CNTL because of the changes of the convective activity associated with the Kilo. It is indicated that the cloud microphysics scheme in models can affect atmospheric thermodynamic fields causing mesoscale convective systems and the forecast

on rainfall amount is quite sensitive to the cloud microphysiscs scheme in this case. It is desired that the uncertainty in the cloud microphysics scheme including the parameterization of ice nuclei should be reduced in the future.

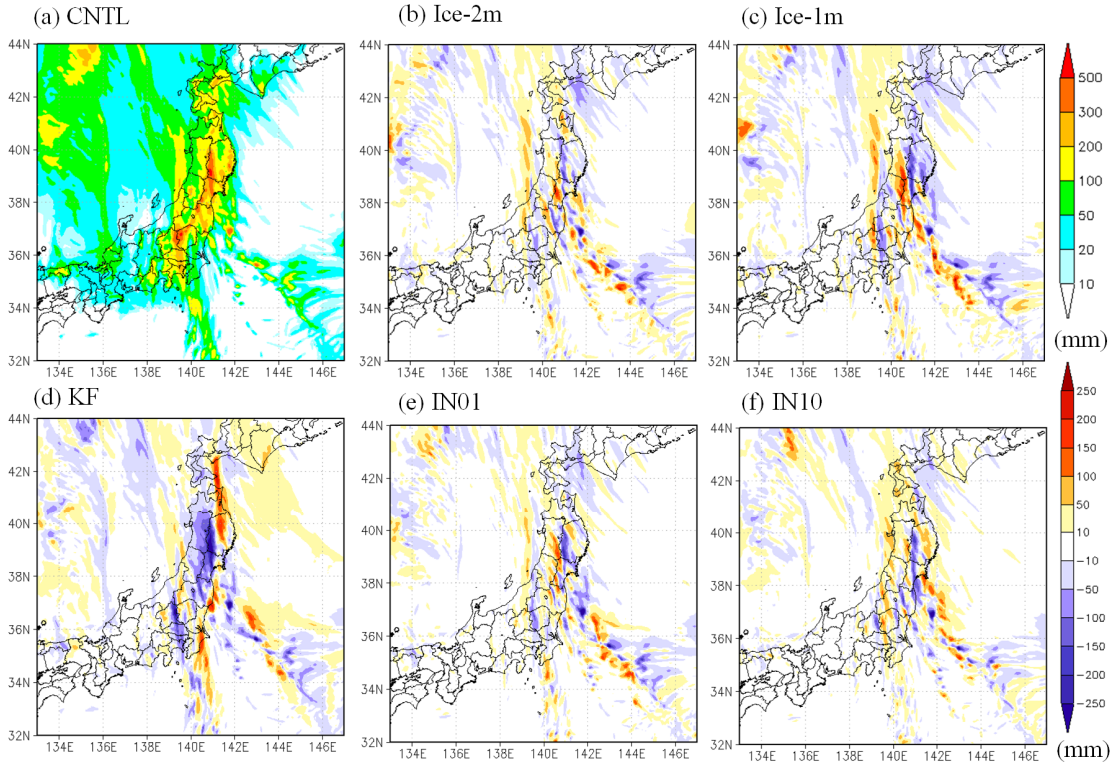

Figure 3. (a) Horizontal distribution of precipitation amounts from 18 UTC on 8 to 00 UTC on 11 September 2015 in CNTL, and the differences from CNTL for each experiment.

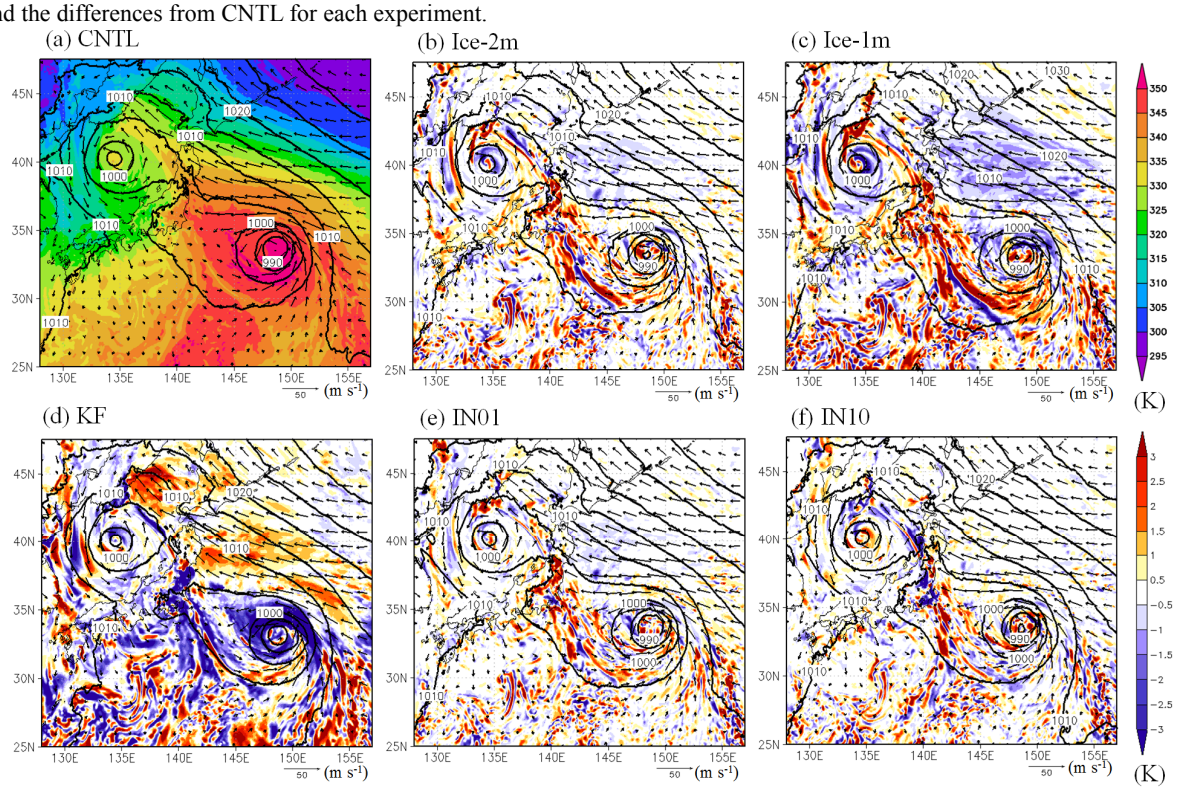

Figure 4. (a) Equivalent potential temperature at 950 hPa at 12 UTC on 10 September in CNTL, and the differences from CNTL for each experiment. Contour lines and vectors respectively indicate sea level pressure (hPa) and horizontal wind at 950 hPa in each experiment.

References:

Araki, K., 2016: Influence of cloud microphysics scheme and ice nuclei on forecasting a heavy snowfall event in Japan associated with the "South-Coast Cyclones". *CAS/JSC WGNE Research Activities in Atmospheric and Oceanic Modelling*, **46**, 4.03–4.04.

Araki, K., and M. Murakami, 2015: Numerical simulation of heavy snowfall and the potential role of ice nuclei in cloud formation and precipitation development. *CAS/JSC WGNE Research Activities in Atmospheric and Oceanic Modelling*, **45**, 4.03–4.04.

The Effect of Radiative Forcings of Various Constituents of the Earth-Atmosphere on the Global Energy Transfer

Z.N. Begum*

**Ex-Scientist 'G'/Advisor, DST, New Delhi; India ;OWSD Full Member , Trieste, Italy.*

(Email: begumzn@hotmail.com)

Chemical tracers and aerosols are micro-particles with mean radii of 10^{-4} to 10^{-6} m. They include gases like CH_4, NO, N_2O, SO_2, NH_3, CO, CO_2, HNO_3, CFC and O_3. Aerosols and the greenhouse gases are essentially important elements of the world climate system. They affect both, the present-day climate as well as the future climate change. Aerosol source gases directly scatter and absorb radiation in cloud-free and cloudy conditions [1]. On the other hand, they indirectly play the role as cloud condensation nuclei (CCN) and modify optical properties of clouds.

The absorption of solar radiation by the aerosol layer increases the radiative heating of the atmosphere, while the fraction of scattering that leaves the atmosphere decreases the total amount of energy available to the earth-atmospheric system [2,3]. The composition of the atmosphere controls the climate to a large extent. In particular, the greenhouse gases in the atmosphere play a crucial role in determining the earth's climate. Thus the different constituents of the earth's atmosphere may interact in complex ways on different space and time.

Significant scattering, including multiple scattering and absorption of radiation can occur in the same part of the atmosphere due to the presence of aerosols and gases (Begum, 1998). The numerical global atmospheric models with comprehensive model physics are the tool for simulation and proper understanding of the feedback mechanism and the radiative forcings. The model used in these experiments is an 'Atmospheric Global Circulation Model' (AGCM) [4], with modified radiation scheme (M-AGCM) [1-3]. In order to compute the global energy balance, radiative transfer processes and their spectral dependence must be treated adequately as the continental aerosols and gases modify the atmospheric physical environment significantly. The magnitude of heating and cooling has changed considerably due to the physical processes and their interaction with the constituents present in the earth-atmospheric system.

Based on the M-AGCM, the optical properties of aerosols and gases are computed. The results of the global energy balance are given in the following Table, which are compared with the radiation budget data collected by the Earth Radiation Budget Experiment (ERBE) on global annual mean basis [5-7].

Table - Global Energy Balance for the month of June 1997

Types of Radiative Fluxes	Global annual mean condition flux (C) (in W/m^{-2}) (Ref. [5-7])	Modified Atmospheric Global Circulation Model (M-AGCM) (in W/m^{-2}) Present work
Incoming solar radiation	343	343
Reflected solar radiation	106	105
Outgoing long-wave radiation (OLR)	237	238
Atmospheric absorption of solar radiation by various constituents	68	70
Latent heat (LH)	90	89
Sensible heat (SH)	16	16
Surface absorption of solar radiation	169	168
Downward long-wave emission	327	325
Upward long-wave emission by the surface	390	388

From these findings we conclude that due to increase in aerosol and greenhouses gas concentrations there is more absorption of radiation in the lower atmosphere as a result of which the global temperature rises gradually.

References

[1] Begum, Z.N., 2005, Modeling of chemical tracer transport in the atmospheric environment and its impact on the global climate. JQSRT , 95,423-7.

[2] Begum Z.N.,2003, A theoretical investigation of the radiative effects and microphysical processes involvrd in the interaction of aerosol particulates in the atmosphere and validation of the theoretical results with INDOEX observations. JQSRT,78;99-103.

[3] Begum, Z.N., 1998, Scattering of solar radiation by aerosol particulates in the atmosphere: a theoretical approach validated with pre- INDOEX. J. Atmos. Sol-Terr Phys, 60, 1751-4.

[4] Kanamitsu, M., 1989. Description of the NMC global data assimilation and forecast system . Weather and Forecasting 4, 335-342.

[5] Ramanathan, V. 1987. The role of earth radiation budget studies in climate and general circulation research. J. Geophys. Res.,92,4075-4095.

[6] Houghton, J.T., Ding, Y., Griggs, D.J., Noguer, M., Linden, P.J.V., and Xiaosu, D. (Eds.), 2001, Climate Change 2001: The Scientific Basis. Contribution of Working Group of the Intergovernmental Panel on Climate Change (IPCC), New York, Cambridge University Press.

[7] Ramanathan, V., Cess, R.D., Harrison, E.F., Minnis, P., Barkstrom, B.R., Ahmed, E., Hartmann, D., 1989, Science 243, (4887), 57-63, Cloud-radiative forcing and climate: Results from the earth radiation budget experiment.

On consequences of measurements of turbulent Lewis number from observations.

by Pascal Marquet⋆, William Maurel† and Rachel Honnert⋆

(WGNE Blue-Book 2017).

Météo-France. ⋆CNRM/GMAP. †CNRM/GMEI. Toulouse. France. *E-mail: pascal.marquet@meteo.fr*

1 Motivations

Almost all parameterizations of turbulence in NWP models and GCM make the assumption of equality of exchange coefficients K_h for heat and K_w water. These two exchange coefficients are applied to the two moist-air Betts (1973) "conservative" variables

$$\theta_l \;=\; \theta \, \exp\left(- \frac{L_v \, q_l \, + \, L_s \, q_i}{c_{pd} \, T} \right) \, , \qquad (1)$$

$$q_t \;=\; q_v \, + \, q_l \, + \, q_i \qquad (2)$$

(where $\theta = T \, (p_0/p)^{R_d/c_{pd}}$ is the dry air potential temperature) to compute the vertical turbulent fluxes written as: $\overline{w' \, \theta'_l} = - K_h \, \partial \overline{\theta_l} / \partial z$ and $\overline{w' \, q'_t} = - K_w \, \partial \overline{q_t} / \partial z$.

However, large uncertainties exists in old papers published in the 1950s, 1960s and 1970s, where the turbulent Lewis number $\mathrm{Le}_t = K_h / K_w$ have been evaluated from observations. Some papers are favourable to the hypothesis $K_h = K_w$ and $\mathrm{Le}_t = 1$, while others have observed higher values, up to $\mathrm{Le}_t > 4$.

Moreover, the use of the Betts variable θ_l is based on an approximate moist-air entropy equation and this formulation has been improved in Hauf and Höller (1987) and Marquet (2011, 2015), where the new potential temperature θ_s is defined as synonymous of the moist-air entropy.

The aim of this note is: 1) to trust the recommendations of Richardson (1919), who suggested to use the moist-air entropy as a variable on which the turbulence is acting; 2) then to replace θ_l by the third-law entropy value θ_s, which must correspond to a new exchange coefficients K_s; 3) compute K_s and $\mathrm{Le}_{ts} = K_s / K_w$ from observations (Météopole-Flux and Cabauw masts) and from LES and SCM outputs for the IHOP case (Couvreux *et al.*, 2005).

2 The moist-air entropy flux

The specific (per unit mass of *moist-air*) entropy is defined in Marquet (2011, 2015) by $s = s_{ref} + c_{pd} \, \ln(\theta_s)$, where s_{ref} and c_{pd} are two constants. If liquid water or ice do not exist, $\theta_l = \theta$ and the first-order approximation of the moist-air entropy potential temperature is $\theta_s \approx \theta \, \exp(\Lambda \, q_v)$, where $\Lambda \approx 5.87$ is a constant which depends on the third-law reference values of entropy of dry air and water vapour. The second-order approximation derived in Marquet (2016) writes

$$\theta_s \;\approx\; \theta \; \exp(\Lambda \, q_v) \; \exp[\, - \gamma \; \ln(r_v / r_*) \, q_v \,] \, , \qquad (3)$$

where $\gamma \approx 0.46$ and $r_* \approx 12.4$ g/kg are two constants.

With Reynolds hypotheses, the flux of moist-air entropy potential temperature can be written as

$$\overline{w' \theta'_s} \;=\; - \, K_s \, \frac{\partial \overline{\theta_s}}{\partial z} \, , \qquad (4)$$

$$\overline{w' \theta'_s} \;\approx\; \exp(\Lambda \, \overline{q_v}) \; \overline{w' \theta'} + \; \overline{\theta_s} \; \left[\, \Lambda - \gamma \; \ln\left(\frac{\overline{r_v}}{r_*} \right) - \frac{\gamma}{1 - \overline{q_v}} \, \right] \; \overline{w' q'_v} \, . \qquad (5)$$

This flux is a weighted sum of the fluxes for θ and q_v. And if the turbulence is to be represented by the flux of θ_s and q_v, the corresponding flux of θ is given by

$$\overline{w' \theta'} \;\approx\; - \, K_w \; \mathrm{Le}_{ts} \; \frac{\partial \overline{\theta}}{\partial z} - \, K_w \; (\mathrm{Le}_{ts} - 1) \; \left[\, \Lambda - \gamma \; \ln\left(\frac{\overline{r_v}}{r_*} \right) - \frac{\gamma}{1 - \overline{q_v}} \, \right] \; \overline{\theta} \; \frac{\partial \overline{q_v}}{\partial z} \, , \qquad (6)$$

where the moist-entropy Lewis turbulent number is $\mathrm{Le}_{ts} = K_s / K_w$.

If $\mathrm{Le}_{ts} = 1$, the second line of (6) cancels out and $K_h = K_s = K_w$ allows to write the flux of θ as $\overline{w' \, \theta'} = - \, K_h \, \partial \overline{\theta} / \partial z$, in terms of the exchange coefficient K_h.

Differently, if $\mathrm{Le}_{ts} \neq 1$, the second line of (6) exists and the flux of θ is not proportional to the sole vertical gradient of θ: it also depends on the vertical gradient of q_v. This prevents defining properly an "exchange coefficient K_h for θ", and the turbulence must clearly be applied to θ_s and q_v, and not to $\theta_l = \theta$ and q_v.

It is thus important to try to determine, from observations and/or from numerical results, whether $\mathrm{Le}_{ts} = 1$ or if Le_{ts} is significantly different from unity?

3 Results

Figures 1 show that average yearly Lewis turbulent numbers computed with the the eddy-correlation method are significantly larger than unity in daytime, and are lower than 1.0 at night. The significant level is more often reached for monthly averages Figures (not shown) and this diurnal cycle is also observed almost each days, with a maximum present just after sunrise.

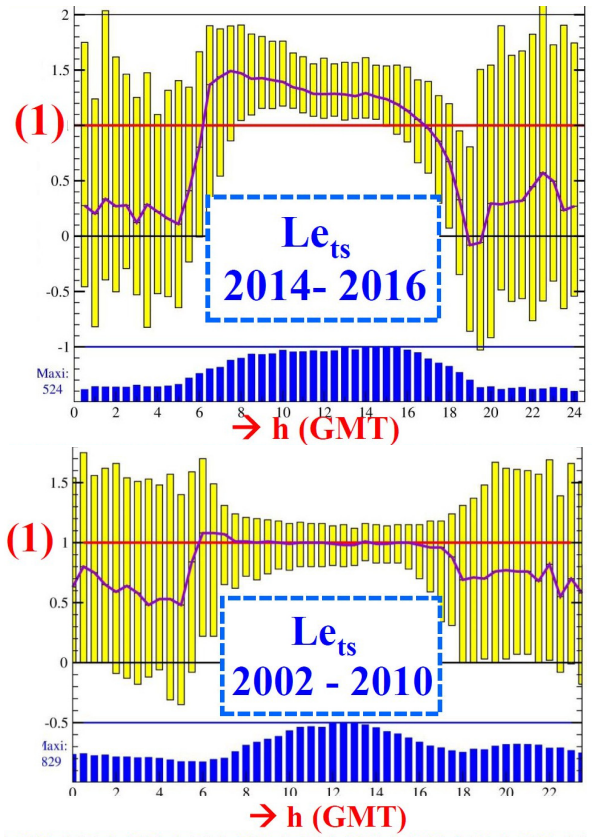

Figure 1: *The boxplots for the Lewis number $Le_{ts} = K_s/K_w$ in terms of the GMT hours. Top: the Météopole-Flux mast for 2 years (CNRM at Toulouse, France). Bottom: thanks to F. Bosvelt, the Cabauw mast for 9 years (KNMI at Utrecht, Holland). The number of observations for each class of GMT hours are in blue vertical bars. The level $Le_{ts} = 1$ is in red and median values are in purple piecewise curve.*

This maximum of Le_{ts} is often larger than 2 in June-August and if often smaller than 0.8 in winter.

The observed diurnal cycle for Le_{ts} may explain the previous disagreements in the articles of the 1970s: values close to 1.0 may be observed in the late afternoon and values larger than unity in the early morning?

Figure 2 shows that the LES outputs for the IHOP case lead to robust computations of the new moist-air entropy exchange coefficient $K_s = -(\overline{w'\theta'_s})/(\partial\overline{\theta_s}/\partial z)$ and of K_w by means of the eddy-correlation method, whereas values of K_h determined from the flux and the vertical gradient of θ is subject to infinite values (due to zero vertical gradient from about 150 to 300 m, depending on the hour) and to a counter-gradient region (due to the same signs of flux and vertical gradient above the level of infinite value).

The turbulent Lewis number is close to 1.0 close to the surface on Figure 2, and then increases with altitude, reaching values above 1.5 above the 150 m height where the mass-flux starts to be active.

4 Conclusion

Values of the turbulent Lewis number significantly smaller or larger than 1.0 are observed for the

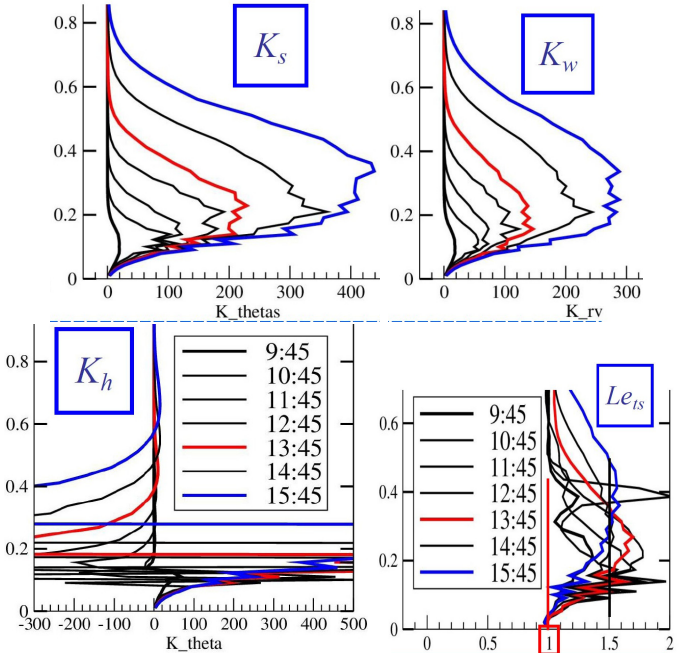

Figure 2: *The vertical profiles of K_s, K_w, K_h and $Le_{ts} = K_s/K_w$ for hourly averages of a LES run for the moist (but clear-air) case IHOP. Heights are in ordinates from 0 to 6 km or 8 km.*

Météopole-Flux and the Cabauw masts, and simulated by a LES of the IHOP case. Consequently, it is necessary to revisit the equations of turbulence and to determined the values of several new constant coefficients (for the pressure and the second-order moment terms). These observations and simulations outputs will be used to compute these coefficients.

References

• Betts AK. (1973). Non-precipitating cumulus convection and its parameterization. *Q. J. R. Meteorol. Soc.* **99** (419): 178–196.

• Couvreux F. *et al.* (2005). Water-vapour variability within a convective boundary-layer assessed by large-eddy simulations and IHOP 2002 observations. *Q. J. R. Meteorol. Soc.* **131** (611): p.2665-2693. `http://dx.doi.org/10.1256/qj.04.167`

• Hauf T. and Höller H. (1987). Entropy and potential temperature. *J. Atmos. Sci.*, **44** (20): p.2887-2901.

• Marquet P. (2011). Definition of a moist entropic potential temperature. Application to FIRE-I data flights. *Q. J. R. Meteorol. Soc.* **137** (656): p.768–791. `http://arxiv.org/abs/1401.1097`

• Marquet P. (2015). An improved approximation for the moist-air entropy potential temperature θ_s. *WGNE Blue-Book*. `http://arxiv.org/abs/1503.02287`

• Marquet P. (2016). The mixed-phase version of moist-air entropy. *WGNE Blue-Book*. `http://arxiv.org/abs/1605.04382`

• Richardson L. F. (1919). Atmospheric stirring measured by precipitation. Proc. Roy. Soc. London (A). 96: p.9-18. `https://ia600700.us.archive.org/32/items/philtrans07640837/07640837.pdf`

On new bulk formulas based on moist-air entropy.

by Pascal Marquet⋆ and Sophie Belamari† (WGNE Blue-Book 2017).

Météo-France. ⋆CNRM/GMAP. †CNRM/GMGEC. Toulouse. France. *E-mail: pascal.marquet@meteo.fr*

1 Motivations

In atmospheric modelling, turbulent air-sea fluxes for the momentum, "heat" and moisture are computed from meteorological variables (wind components u and v, dry-air potential temperature θ and water vapour specific content q_v) using bulk formulas.

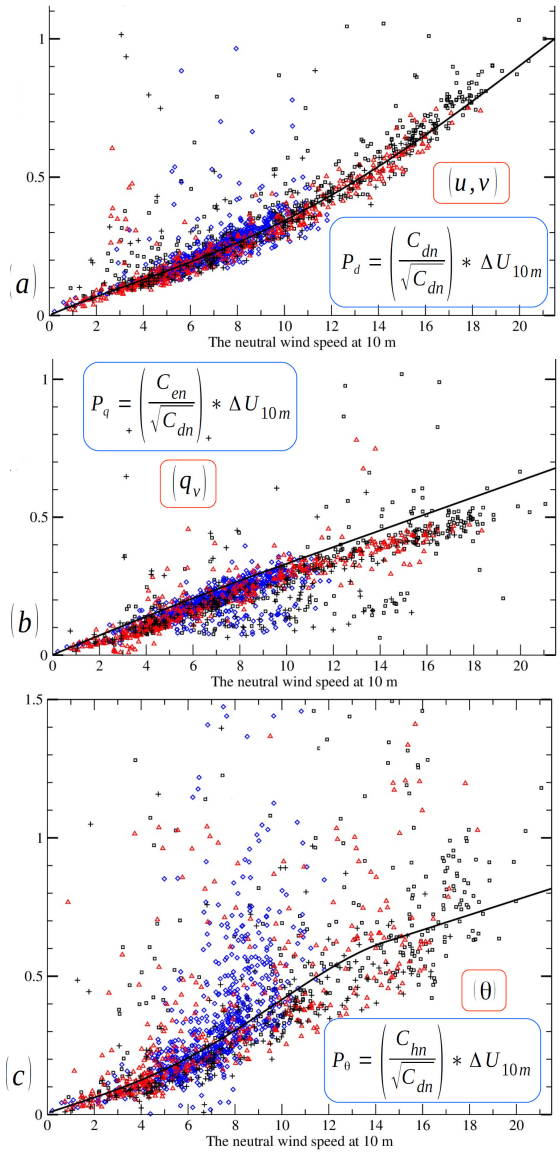

Figure 1: *Scatter-plots of the speed scales equivalent parameters: (a) P_d, (b) P_q and (c) P_θ derived from the neutral exchange coefficients C_{dn}, C_{en} and C_{hn} for the CATCH (black square), EQUALANT (blue diamond), FETCH (red triangle up) and POMME (black plus) experiments.*

In the surface modelling platform SURFEX (Masson et al. 2013, Le Moigne 2013) used by both the AROME NWP model and ARPEGE GCM, these bulk formulas rely on the ECUME parameterization derived from several campaigns, namely CATCH, EQUALANT, FETCH, SEMAPHORE, POMME and EGEE (Belamari and Pirani 2007, Belamari et al. 2016).

While previous versions of the ECUME parameterization provided analytical formulations (as a function of the neutral wind speed at 10 m hereafter referred to as $U_{10\mathrm{m}}$) for the neutral exchange coefficients (drag coefficient C_{dn} for the momentum, Stanton number C_{hn} for the "heat" or θ, and Dalton number C_{en} for the moisture), the current version provides formulations for "speed scales equivalent parameters" P_d, P_θ and P_q derived from these neutral exchange coefficients.

As shown in Figures 1 (a,b,c), the scattering of the points appears as much more important for the dry-air potential temperature speed scale equivalent parameter P_θ when compared to those of both the wind (P_d) and water-vapour specific content (P_q). Moreover, it is observed that the fitted curves for $P_\theta(U_{10\mathrm{m}})$ and $P_q(U_{10\mathrm{m}})$ are different: this means that the Lewis turbulent number, which is the ratio of C_{hn} over C_{en}, and therefore of P_θ over P_q, is greater than unity.

The aim of this note is triple: 1) to trust the recommendations of Richardson (1919) who suggested to use the moist-air entropy as a variable on which the turbulence is acting; 2) to introduce the moist-air entropy potential temperature θ_s derived in Marquet (2011, 2015) instead of the current dry-air potential temperature θ; and 3) to give insights on the dispersion noticed in the scatter-plot obtained for P_θ (Figure 1 c).

2 The moist-air entropy fluxes

The specific value (i.e. per unit mass of *moist-air*) of the moist-air entropy is defined in Marquet (2011, 2015) by $s = s_{ref} + c_{pd}\ \ln(\theta_s)$, where θ_s denotes the moist-air entropy potential temperature, and s_{ref} and c_{pd} are two constants.

If liquid water or ice does not exist, a first-order approximation of the moist-air entropy potential temperature is given by $\theta_s \approx \theta\ \exp(\Lambda\ q_v)$, where $\Lambda \approx 6$ is a constant which depends on the third-law reference values of entropy of dry air and water vapour. The flux of moist-air entropy potential temperature defined as:

$$\overline{w'\theta'_s} = \rho\ C_{sn}\ U_{10m}\ (\Delta\theta_s)_{10m} \qquad (1)$$

can thus be written as:

$$\overline{w'\theta'_s} \approx \exp(\Lambda\ \overline{q_v})\ \overline{w'\theta'} + \Lambda\ \overline{\theta_s}\ \overline{w'q'_v}\,, \qquad (2)$$

i.e. as the weighted sum of the fluxes of θ and q_v:

$$\overline{w'\theta'} = \rho\ C_{hn}\ U_{10m}\ (\Delta\theta)_{10m}\,, \qquad (3)$$

and $\overline{w'q'_v} = \rho\ C_{en}\ U_{10m}\ (\Delta q_v)_{10m}$, (4)

respectively.

If the turbulence is represented by the fluxes of θ_s and q_v (Eqs.(1) and (4), respectively), one can then derive from Eq.(2) the corresponding flux of θ:

$$\overline{w'\theta'} \approx (\mathrm{Le}_{ts})\ [\rho\ C_{en}\ U_{10m}\ (\Delta\theta)_{10m}] + (\mathrm{Le}_{ts} - 1)\ \Lambda\ \overline{\theta}\ \overline{w'q'_v}, \quad (5)$$

where $\mathrm{Le}_{ts} = C_{sn}/C_{en}$ denotes the moist-entropy Lewis turbulent number. If $\mathrm{Le}_{ts} \neq 1$, the second line of (5) exists and the flux of θ is not proportional to the vertical gradient $(\Delta\theta)_{10m}/\Delta z$. This prevents defining a Stanton number C_{hn}, and this may explain why the scatter-plot obtained for P_θ is so noisy in Figure 1 (c).

3 Results

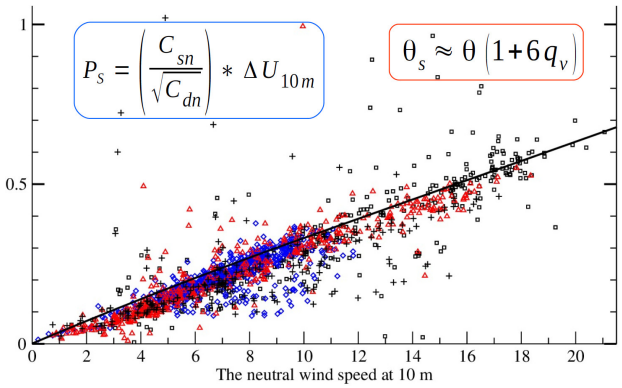

Figure 2: *Same as Fig. 1 (c) but for P_s and C_{sn}.*

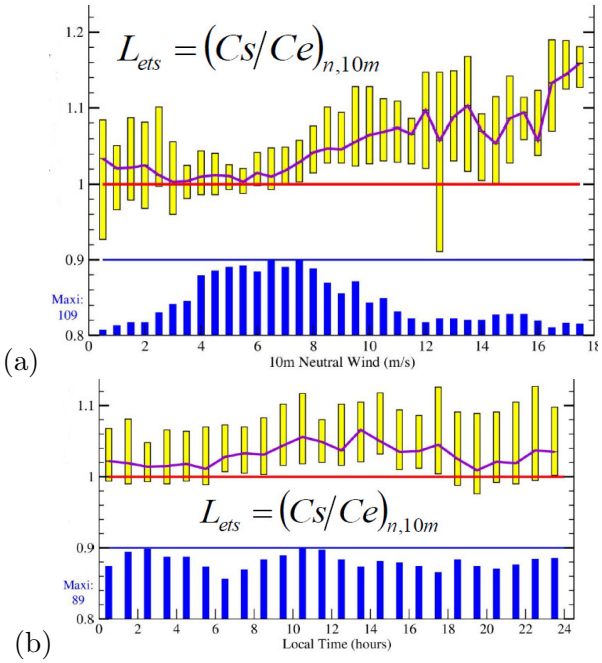

Figure 3: *Boxplots for the moist-entropy Lewis turbulent number $\mathrm{Le}_{ts} = C_{sn}/C_{en}$ in terms of (a) $U_{10\mathrm{m}}$ and (b) the UTC local time. The number of observations for each class of wind speed or hours is indicated in blue.*

Figure 2 shows that the scattering of the $P_s(U_{10\mathrm{m}})$ points is much smaller than that of the $P_\theta(U_{10\mathrm{m}})$ points, and is similar to those obtained for the $P_d(U_{10\mathrm{m}})$ and $P_q(U_{10\mathrm{m}})$ points.

Figures 3 (a,b) indicate that the moist-entropy Lewis turbulent number Le_{ts} is often significantly different from unity, especially for small (< 2 m/s) and large (> 8 m/s) wind speeds (Fig. 3 a), as well as for day-time hours (from 8 to 18 h, Fig 3 b).

4 Conclusion

The results shown in Figures 2 and 3 sustain that the observations of CATCH, EQUALANT, FETCH and POMME experiments confirm that the moist-air entropy potential temperature θ_s is a better candidate than the dry-air value θ for applying turbulent processes over oceans.

The mean values of the moist-air entropy turbulent Lewis number Le_{ts} plotted in Figures 3 against the wind speed $U_{10\mathrm{m}}$, and/or the local UTC hours, might serve to build a new parameterization for the moist-air entropy potential temperature flux, from which the typical air-sea "sensible heat" flux may be thereafter derived from Eq.(5).

References

• Belamari S. and Pirani A. (2007). Validation of the optimal heat and momentum fluxes using the ORCA2-LIM global ocean-ice model Deliverable D4.1.3 Marine Environment and Security for the European Area - Integrated Project (MERSEA IP).

• Belamari S. *et al.* (2016). Vers une nouvelle représentation des flux turbulents océan-atmosphère : la paramétrisation ECUME revisitée. Ateliers de Modélisation de l'Atmosphère. Toulouse. `http://www.meteo.fr/cic/meetings/2016/AMA/presentations/2016/Dephy_jeudi/06-2016-01-21_expose_AMA_Belamari.pdf`

• Marquet P. (2011, M11). Definition of a moist entropic potential temperature. Application to FIRE-I data flights. *Q. J. R. Meteorol. Soc.* **137** (656): p.768–791. `http://arxiv.org/abs/1401.1097`

• Marquet P. (2015, M15). An improved approximation for the moist-air entropy potential temperature θ_s. *WGNE Blue-Book*. `http://arxiv.org/abs/1503.02287`

• Masson V. *et al.* (2013). The SURFEXv7.2 land and ocean surface platform for coupled or offline simulation of earth surface variables and fluxes. Geosci. Model Dev. 6 (4): 929-960. `http://www.geosci-model-dev.net/6/929/2013/gmd-6-929-2013.pdf`

• Le Moigne P. (2013). See section 2.2 in the Supplement of the previous paper: `http://www.geosci-model-dev.net/6/929/2013/gmd-6-929-2013-supplement.pdf`

• Richardson L. F. (1919). Atmospheric stirring measured by precipitation. Proc. Roy. Soc. London (A). 96: p.9-18. `https://ia600700.us.archive.org/32/items/philtrans07640837/07640837.pdf`

The impacts of observed small turbulent Lewis number in stable stratification: changes in the thermal production?

by Pascal Marquet. WGNE Blue-Book 2017.

Météo-France. CNRM/GMAP. Toulouse. France.

E-mail: pascal.marquet@meteo.fr

1 Motivations

It is shown in Marquet *et al.* (2017a,b) that the assumption of equality of exchange coefficients K_h for heat, K_w for water and K_s for entropy is not supported by observations.

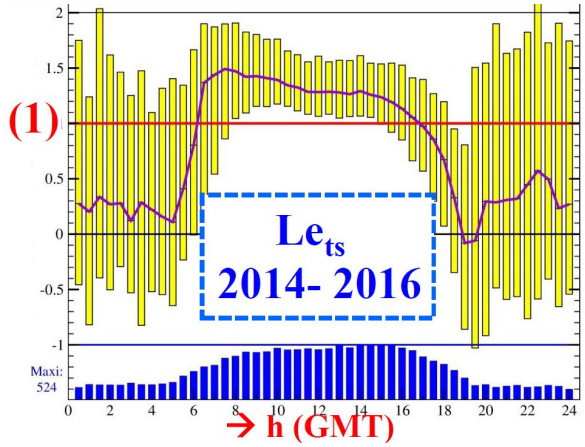

Figure 1: *The boxplots (yellow interquartile range) for the moist-entropy turbulent Lewis number* $Le_{ts} = K_s/K_w$ *in terms of the GMT hours for the the Météopole-Flux mast and for a 2 years average (CNRM at Toulouse, France). The number of observations for each class of hours are in blue vertical bars. The level* $Le_{ts} = 1$ *is in red and median values are in purple piecewise curve.*

As an example, Figure 1 shows that yearly average values of the moist-entropy Lewis turbulent number $\mathrm{Le}_{ts} = K_s/K_w$ are significantly larger than unity in daytime, and are lower than 0.5 at night. Moreover, values of Le_{ts} may reach the zero level for stable stratifications (here between 19 and 20 GMT).

The consequences of $\mathrm{Le}_{ts} = K_s/K_w \approx 0$ are derived in this note in terms of the thermal production $\beta\ \overline{w'\theta'_v}$, which is one of the terms forming the turbulent kinetic energy equation, where $\beta = g/\theta_0$ and where the virtual potential temperature is $\theta_v = \theta\ (1+\delta\, q_v - q_l - q_i)$, with $\delta \approx 0.6$ and $\theta = T\ (p_0/p)^{R_d/c_{pd}}$.

To make simple, and in order to simulate moist and cloud-free conditions like the IHOP case (Couvreux *et al.*, 2005), condensed water will be neglected in this preliminary study, leading to $q_l + q_i = 0$ and to

$$\boxed{\theta_v \ = \ \theta\ (1 \ + \ \delta\, q_v)}\ . \qquad (1)$$

The Betts (1973) moist variables are then equal to $\theta_l = \theta$ and $q_t = q_v$ and the first-order approximation of the moist-entropy potential temperature defined in Marquet (2011, 2015, 2016) can be written as

$$\theta_s \ \approx \ \boxed{(\theta_s)_1 \ = \ \theta\ \exp(\Lambda\, q_v)}\ , \qquad (2)$$

where $\Lambda \approx 6$ and $(\theta_s)_1 \approx \theta\ (1 + \Lambda\, q_v)$

2 Computation of $\overline{w'\theta'_v}$

The differentials of Eqs. (1) and (2) are

$$d\theta_v \ = (1 + \delta\, q_v)\, d\theta \ + \ \delta\, \theta\, dq_v\ , \qquad (3)$$

$$d(\theta_s)_1 \ = \exp(\Lambda\, q_v)\, d\theta \ + \ \Lambda\, (\theta_s)_1\, dq_v\ . \qquad (4)$$

From Eq. (4) the differential of θ can be computed as $d\theta = \exp(-\,\Lambda\, q_v)\ d(\theta_s)_1 \ - \ \Lambda\ \theta\ dq_v$. This expression can then be inserted into Eq. (3) to give

$$\begin{aligned} d\theta_v \ = \ & (1 + \delta\, q_v)\ \exp(-\,\Lambda\, q_v)\ d(\theta_s)_1 \\ & - \ [\ (\Lambda \ - \ \delta) \ + \ \Lambda\, \delta\, q_v\ ]\ \theta\ dq_v\ . \end{aligned} \qquad (5)$$

By applying Reynolds hypotheses, the vertical flux $\overline{w'\theta'_v}$ can be computed from Eq. (5) in terms of the vertical fluxes of $(\theta_s)_1$ and q_v, leading to

$$\begin{aligned} \overline{w'\theta'_v} \ = \ & (1 + \delta\, \overline{q_v})\ \exp(-\,\Lambda\, \overline{q_v})\ \overline{w'(\theta'_s)_1} \\ & - \ [\ (\Lambda \ - \ \delta) \ + \ \Lambda\, \delta\, \overline{q_v}\ ]\ \overline{\theta}\ \overline{w'q'_v}\ , \end{aligned} \qquad (6)$$

$$\text{and} \quad \overline{w'\theta'_v} \ \approx \ \overline{w'(\theta'_s)_1} \ - \ 5.4\ \overline{\theta}\ \overline{w'q'_v}\ . \qquad (7)$$

The approximate flux (7) is obtained with the assumptions $1 + 0.6\ \overline{q_v} \ \approx \ 1$, $\exp(-\ 6\ \overline{q_v}) \ \approx \ 1$ and $6 \ \times \ 0.6\ \ \overline{q_v} \ \ll 6 - 0.6 \ \approx \ 5.4$. The same approximation can be used to derive a similar expression for the vertical derivatives, leading to

$$\frac{\partial \overline{\theta_v}}{\partial z} \ \approx \ \frac{\partial \overline{(\theta_s)_1}}{\partial z} \ - \ 5.4\ \overline{\theta}\ \frac{\partial \overline{q_v}}{\partial z}\ . \qquad (8)$$

3 $\overline{w'\theta'_v}$ expressed in terms of Le_{ts}

According to Richardson (1919), the turbulence is applied to the total water content ($q_t = q_v$) and to the moist entropy variable $(\theta_s)_1$. Accordingly, it is assumed that the vertical fluxes of $(\theta_s)_1$ and q_v can be

expressed in terms of the (positive) exchange coefficients K_s and K_w, leading to

$$\overline{w'(\theta'_s)_1} \approx - K_s \frac{\partial \overline{(\theta_s)_1}}{\partial z} = - K_w \, \mathrm{Le}_{ts} \frac{\partial \overline{(\theta_s)_1}}{\partial z} , \quad (9)$$

$$\overline{w'q'_v} \approx - K_w \frac{\partial \overline{q_v}}{\partial z} , \quad (10)$$

where $\mathrm{Le}_{ts} = K_s/K_w$ is the turbulent Lewis number.

Eqs. (9) and (10) can then be inserted into (7), leading to the two alternative formulations:

$$\overline{w'\theta'_v} \approx - K_w \left[\mathrm{Le}_{ts} \frac{\partial \overline{(\theta_s)_1}}{\partial z} - 5.4 \, \overline{\theta} \, \frac{\partial \overline{q_v}}{\partial z} \right] \quad (11)$$

or, from (8):

$$\overline{w'\theta'_v} \approx - K_w \left[\frac{\partial \overline{\theta_v}}{\partial z} + (\mathrm{Le}_{ts} - 1) \frac{\partial \overline{(\theta_s)_1}}{\partial z} \right] . \quad (12)$$

The second formulation (12) shows that the assumptions $\mathrm{Le}_{ts} = 1$ and $K_s = K_h = K_w$ (made in all present RCMs, NWP models and GCMs parameterizations of turbulence) correspond to a cancellation of the second term into brackets, and then to

$$\boxed{\left(\overline{w'\theta'_v}\right)_{\mathrm{Le}_{ts}=1} \approx - K_w \frac{\partial \overline{\theta_v}}{\partial z} = - K_h \frac{\partial \overline{\theta_v}}{\partial z} .} \quad (13)$$

For very stable conditions and for the present assumption $\mathrm{Le}_{ts} = 1$, then $\partial \overline{\theta_v}/\partial z \gg 0$ and the thermal production $\beta \, \overline{w'\theta'_v}$ is negative due to $\beta = g/\theta_0 > 0$ and to $- K_w < 0$. These negative values for $\overline{w'\theta'_v}$ lead to a rapid extinction of turbulence via the turbulent kinetic energy equation $\partial e/\partial t = \beta \, \overline{w'\theta'_v} + \ldots$.

Differently, values $\mathrm{Le}_{ts} = K_s/K_w \approx 0$ observed in Figure 1 at night and for stable conditions can be inserted into the first formulation (11), leading to a cancellation of the first term into brackets and to

$$\boxed{\left(\overline{w'\theta'_v}\right)_{\mathrm{Le}_{ts}=0} \approx + K_w \, (5.4 \, \overline{\theta}) \, \frac{\partial \overline{q_v}}{\partial z} .} \quad (14)$$

This is a drastic and very important change in the nature of turbulence in stable conditions: if $\mathrm{Le}_{ts} \approx 0$, the thermal production no longer depends on $\partial \overline{\theta_v}/\partial z$ and, rather, $\beta \, \overline{w'\theta'_v}$ only depends on the sign of the vertical gradient of water vapour content $\partial \overline{q_v}/\partial z$!

The physical consequence is that, for $\mathrm{Le}_{ts} \approx 0$, the turbulence may be maintained despite positive values of $\partial \overline{\theta_v}/\partial z$ (which have no impact) and precisely in those regions where $\partial \overline{q_v}/\partial z$ is positive.

Intermediate values of Le_{ts} between 0 and 1 (or above 1) would imply a mixed influence of the two vertical gradients of $\overline{q_v}$ and $\overline{\theta_v}$.

4 Conclusion

Observations of small or null values of the turbulent Lewis number $\mathrm{Le}_{ts} = K_s/K_w$ at night and in stable and moist conditions may have a large impact on the thermal production and the vertical flux $\overline{w'\theta'_v}$.

It is shown that $\mathrm{Le}_{ts} \approx 0$ means that $\overline{w'\theta'_v}$ becomes proportional to (and is of the same sign as) the vertical gradient of water vapour content $\partial \overline{q_v}/\partial z$, with a factor ($5.4 \, \overline{\theta}$) which is of the order of $5.4 \times 300 \approx 1600$. This means that a moderate vertical change of $\Delta \overline{q_v} = +1$ g/kg in (14) would have a large impact corresponding to positive and significant values of thermal production, an impact similar to the one created by an unstable value $\Delta \overline{\theta_v} = -1.6$ K in (13) for $\mathrm{Le}_{ts} = 1$.

The behaviour of present turbulent kinetic equations might be improved by taking into account Eq. (14) in stable and moist conditions. It is thus needed to revisit the theoretical formulations of K_s and K_w in existing RCMs, NWP models and GCMs parameterizations of turbulence, with the need to represent Lewis numbers different from 1 and depending on the local stability.

References

• Betts AK. (1973). Non-precipitating cumulus convection and its parameterization. *Q. J. R. Meteorol. Soc.* **99** (419): 178–196.

• Couvreux F. *et al.* (2005). Water-vapour variability within a convective boundary-layer assessed by large-eddy simulations and IHOP 2002 observations. *Q. J. R. Meteorol. Soc.* **131** (611): p.2665-2693. http://dx.doi.org/10.1256/qj.04.167

• Hauf T. and Höller H. (1987). Entropy and potential temperature. *J. Atmos. Sci.*, **44** (20): p.2887-2901.

• Marquet P. (2011). Definition of a moist entropic potential temperature. Application to FIRE-I data flights. *Q. J. R. Meteorol. Soc.* **137** (656): p.768–791. http://arxiv.org/abs/1401.1097

• Marquet P. (2015). An improved approximation for the moist-air entropy potential temperature θ_s. *WGNE Blue-Book*. http://arxiv.org/abs/1503.02287

• Marquet P. (2016). The mixed-phase version of moist-air entropy. *WGNE Blue-Book*. http://arxiv.org/abs/1605.04382

• Marquet P., Maurel W. and Honnert R. (2017a). On consequences of measurements of turbulent Lewis number from observations. *WGNE Blue-Book*.

• Marquet P., Belamari S. (2017b). On new bulk formulas based on moist-air entropy. *WGNE Blue-Book*.

• Richardson L. F. (1919). Atmospheric stirring measured by precipitation. Proc. Roy. Soc. London (A). 96: p.9-18. https://ia600700.us.archive.org/32/items/philtrans07640837/07640837.pdf

Stormscale-mesoscale physics parameterization suite for the NOAA 3km HRRR and 13km RAP models and other applications

Joseph B. Olson, Georg Grell, Tatiana Smirnova, Jaymes Kenyon,
John Brown, Curtis Alexander, Stan Benjamin
NOAA Earth System Research Laboratory, Boulder, Colorado USA. Joseph.B.Olson@noaa.gov

RAPv4/HRRRv3 Summary of Changes

Implementation RAPv4/HRRRv3 - NCEP planned in Feb 2018

Updated for RAPv4/HRRRv3

WRF-ARW hybrid vertical coordinate. Advanced physics.

VIIRS real-time greenness vegetation fraction.

Model	Run at:	Domain	Grid Points	Grid Spacing	Vertical Levels	Pressure Top	Boundary Conditions	Initialized
RAP	GSD, NCEP	North America	953 x 834	13 km	50	10 hPa	GFS	Hourly (cycled)
HRRR	GSD, NCEP	CONUS	1799 x 1059	3 km	50	20 hPa	RAP	Hourly (pre-forecast hour cycle)

Model	Version	Assimilation	Radar DA	Radiation LW/SW	Microphysics	Cumulus Param	PBL	LSM
RAP	WRF-ARW v3.9 - hyb	GSI Hybrid Ens to 0.85, better cloud	13-km DFI ½ strength	RRTMG/ RRTMG	Thompson Aerosol v3.9	GF + Shallow	MYNN v3.9	RUC v3.9
HRRR	WRF-ARW v3.9 - hyb	GSI Hybrid En to 0.85, better cloud	3-km 15-min LH	RRTMG/ RRTMG	Thompson Aerosol v3.9	None	MYNN v3.9	RUC v3.9

Model	Horiz/Vert Advection	Scalar Advection	Upper-Level Damping	6th Order Diffusion	SW Radiation Update	Land Use	MP Tend Limit	Time-Step
RAP	5th/5th	Positive-Definite	w-Rayleigh 0.2	Yes 0.12	20 min	15" MODIS Seasonal	0.01 K/s	60 s
HRRR	5th/5th	Positive-Definite	w-Rayleigh 0.2	Yes -0.25 (slope dep)	15 min with SW-dt	15" MODIS Seasonal	0.07 K/s	20 s

Fig 1. Characteristics including physical parameterizations for 3km HRRRv3 and RAPv4, expected for implementation at NCEP in February 2018. Key changed areas are shaded in orange.

The physics parameterization suite used in NOAA for the 3km High-Resolution Rapid Refresh (**HRRR**) and 13km Rapid Refresh (**RAP**) hourly updated models has been refined over the past few years for all-season boundary-layer forecasting including clouds, precipitation, and convective environment. Both physics and data assimilation refinements have contributed to the improved near-surface and upper-air skill as shown in Benjamin et al 2016 (B16). The HRRR and RAP models were recently updated (HRRRv2/RAPv3) at NOAA/NCEP in August 2016. An overall description of the RAPv3/HRRRv2 configuration for model and assimilation details are described in B16. Specifically, the HRRR/RAP physics suite is described in B16, section 3.

In 2017, a yet further improved set of physical parameterizations has been developed for RAPv4 and HRRRv3 with this set of physics changes (Fig. 1) results in consistent improved upper-air forecast skill (Fig. 2). The most important parameterization improvements in RAPv4/HRRRv3 are those for the MYNN boundary scheme, the Thompson-Eidhammer cloud microphysics scheme, and the RUC land-surface model.

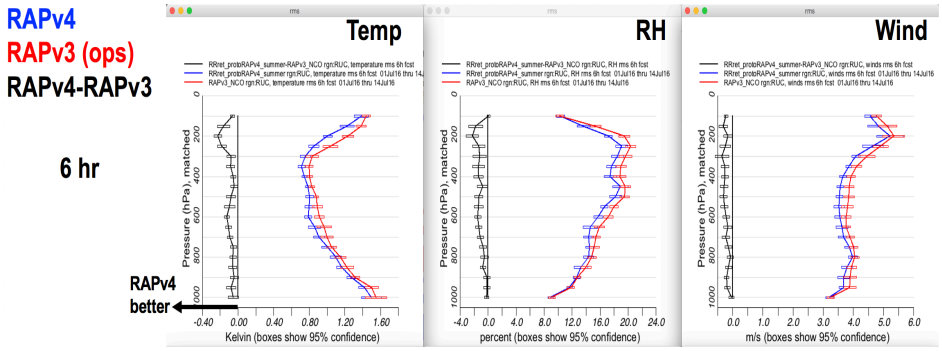

Fig 2. RMS error in temp/RH/wind 6h forecasts vs.raobs from RAPv4 (blue) vs. RAPv3 (red) for July 2016. Improvements to RAP (RAPv4) and HRRR (HRRRv3) models are expected in early 2018 at NOAA/NCEP.

The HRRR and RAP models use this common suite of physical parameterizations with yearly improvements:

1. Grell-Freitas convection – deep and shallow (Grell and Freitas 2014).
2. MYNN PBL – Olson/Kenyon improvements for WRFv3.9 (B16, App. B)
3. RUC land-surface model - 9 soil layers, 2 snow layers - WRFv3.9 version (B16, Smirnova et al 2016). Now includes use of VIIRS greenness vegetation fraction.
4. Thompson aerosol-aware cloud microphysics (Thompson and Eidhammer 2014).

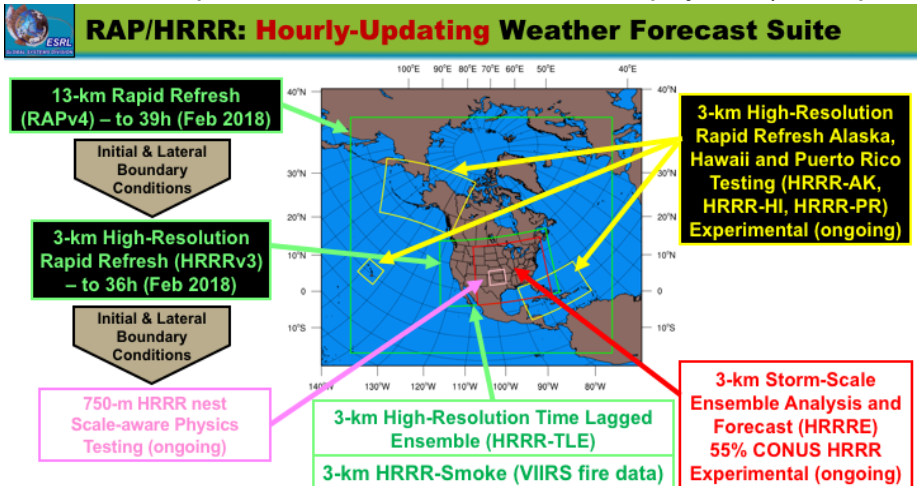

Fig 3. Experimental versions of 3km HRRR and running at NOAA Earth System Research Lab, with Feb 2018 upgrade of operational version of HRRR model at NCEP.

The experimental versions of the RAP and HRRR models described to the left in Fig. 3 all use the new RAPv4/HRRRv3 physics suite shown in Fig. 1.

Benjamin, S. G., S.S. Weygandt, M. Hu, C.A. Alexander, T.G. Smirnova, J.B. Olson, J.M. Brown, E. James, D.C. Dowell, G.A. Grell, H. Lin, S.E. Peckham, T.L. Smith, W.R. Moninger, G.S. Manikin, **2016**, A North American hourly assimilation and model forecast cycle: The Rapid Refresh. *Mon. Wea. Rev.*, **144**, 1669-1694. http://dx.doi.org/10.1175/MWR-D-15-0242.1

Grell, G.A., and S. Freitas, **2014**: A scale and aerosol aware stochastic convective parameterization for weather and air quality modeling. *Atmos. Chem. Phys.*, **14**, 5233-5250, doi:10.5194/acp-14-5233-2014.

Smirnova, T.G., J.M. Brown, and S.G. Benjamin, **2016**: Modifications to the Land Surface Model in the transition from the Rapid Update Cycle (RUC) to the WRF-based Rapid Refresh (RAP). *Mon. Wea. Rev., **144**,* 1851-1865. http://dx.doi.org/10.1175/MWR-D-15-0198.1 .

Thompson, G., and T. Eidhammer, **2014**: A study of aerosol impacts on clouds and precipitation development in a large winter cyclone. *J. Atmos. Sci.*, **71**, 3636-3658, doi: http://dx.doi.org/10.1175/JAS-D-13-0305.1.

Development of a multi-species aerosol-radiation scheme in JMA's global model

Shoukichi Yabu[1], Taichu Y. Tanaka[2] and Naga Oshima[2]

1: Numerical Prediction Division, Japan Meteorological Agency, Tokyo, Japan
2: Meteorological Research Institute, Tsukuba, Ibaraki, Japan
e-mail: yabu@met.kishou.go.jp

1. Introduction

In the aerosol-radiation scheme of the Global Spectral Model (GSM) used by the Japan Meteorological Agency (JMA), the monthly climatology for aerosol total optical depth (ATOD) is based on the total-column value from Moderate Resolution Imaging Spectroradiometer (MODIS), Multi-angle Imaging Spectroradiometer (MISR) and Ozone Monitoring Instrument (OMI) observation data with seasonal variations. In the previous scheme, other optical properties of aerosols (such as the single scattering albedo (SSA) and asymmetry factor (ASF)) were specified as identical background values of continental and maritime types with no seasonal variation in line with WMO (1986), and it was insufficient to represent a radiative effect on aerosols consisting of different chemical species depending on locations. To address this problem, JMA developed a new aerosol radiation scheme allowing consideration of five aerosol types (sulfate, black carbon, organic carbon, sea salt and mineral dust) and their radiative properties.

2. Outline of the new scheme

The five aerosol types specified above are considered in the new aerosol radiation scheme, with mineral dust and sea salt having 6- and 2-size bins, respectively. The three-dimensional monthly climatological distributions of aerosol mass concentrations were derived from a climatological run of the Meteorological Research Institute aerosol transport model (MASINGAR mk-2, Yukimoto et al. 2011), and ATOD distribution is adjusted to the above satellite-based climatology because no aerosol data assimilation was conducted in this derivation.

Radiative parameters corresponding to the new aerosol types (e.g., extinction coefficient, SSA and ASF) were derived via Mie scattering calculation, in which size distribution parameters and the complex refractive indices of each type are generally obtained from the Optical Properties of Aerosols and Clouds (OPAC) database (Hess et al. 1998) and partly taken from recent aerosol observation data. Hygroscopic growth factors of aerosol due to water uptake depend on relative humidity, and are derived from the κ-Köhler theory (Petters and Kreidenweis 2007). All aerosol types are assumed to be externally mixed, and SSA and ASF parameters for all types are averaged and utilized in model radiative computation.

3. Impact of the new scheme on the global atmospheric model climate

To evaluate impact of the new scheme on GSM climatology, 10-year cases of one-month prediction experiments were conducted with a low-resolution (TL479) version of the model and analytically prescribed land/sea surface conditions. The 10 cases of monthly mean prediction data were averaged to give a rough estimate of the model's monthly climatology. Below, NEW (OLD) represents the experiment using the GSM with the new (previous) aerosol radiation scheme.

Figure 1 shows clear-sky downward longwave (LW) radiation flux at the surface compared to the Clouds and the Earth's Radiant Energy System (CERES) observation-based climatology. Around the Sahara Desert and the Arabian Peninsula, values increase by about 10 W/m^2 in the new scheme due to a warmer tropospheric atmosphere caused by enhanced absorption of shortwave (SW) radiation flux by mineral dust aerosols. More realistic representation of SW absorption by mineral dust in NEW is considered to improve downward LW radiation flux shortages of the model in clear-sky conditions.

Figure 2 shows differences in 850 hPa temperature (T850), sea level pressure (Psea) and precipitation amount (Rain) between OLD and NEW (first week mean). It can be seen that T850 is raised in some locations from North Africa to the Middle East due to enhanced SW absorption of mineral dust. A raised T850 area is also seen in the southeast Atlantic, where light-absorbing carbonaceous aerosols originating from biomass burning in Central Africa are distributed in NEW. The impact of aerosol light-absorption on temperature is higher in the downward direction in the troposphere, inducing more unstable atmospheric conditions. This causes cyclonic circulation anomalies over the desert area and the eastern part of the Central Atlantic Ocean (areas with negative Psea difference as shown in Fig. 2 b). These changes also affect wider atmospheric circulation conditions in the model, inducing the modification of precipitation climatology in some tropical areas. In the tropical Atlantic Ocean, a contrast in increased precipitation near the African Continent and decreased precipitation near the Southern American Continent is shown, representing weaker Walker circulation in the Atlantic caused by enhanced light absorption due to mineral dust aerosol (as noted by Lau et al. (2009)).

4. Impact of the new scheme on GSM forecast performance

Short-range forecast experiments were also conducted with atmospheric data assimilation using a subset of the operational analysis and prediction system and a high-resolution (TL959) version of the GSM. Here, TEST (CNTL) refers to the GSM experiment with the new (previous) aerosol-radiation scheme. Figure 3 shows relative improvement in various forecast skill scores of TEST against CNTL for August and January 2015. Numerous scores for the tropics and the summer hemisphere are significantly improved, suggesting that enhanced light absorption by aerosols has a positive influence on model performance both in the tropical region and in the middle latitudes via the modulation of global atmospheric circulation.

In May 2017, the new aerosol-radiation scheme was introduced into the new operational GSM.

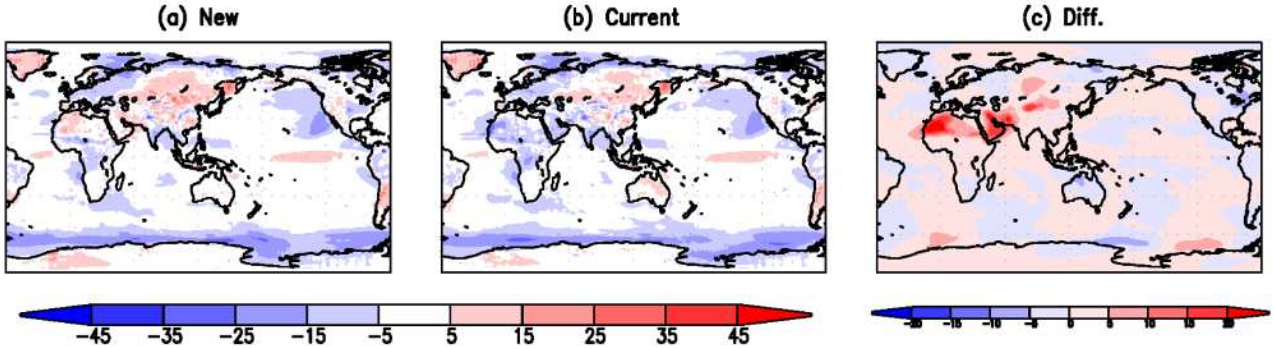

Fig. 1 Climatological difference of clear-sky downward longwave radiation flux at the surface in July: (a) Experiment using the GSM with the new aerosol-radiation scheme (NEW) minus CERES observational climatology; (b) experiment using the GSM with the previous scheme (OLD) minus CERES; and (c) NEW − OLD. Units are W/m^2.

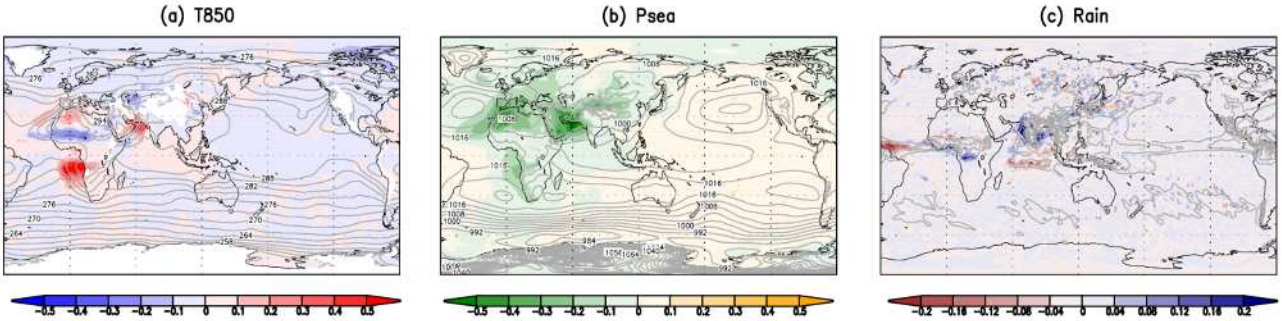

Fig. 2 Climatological difference of (a) 850 hPa temperature [K], (b) sea level pressure [hPa] and (c) precipitation [mm/day] for July. Shading indicates NEW − OLD, and contours show climatological distributions of OLD.

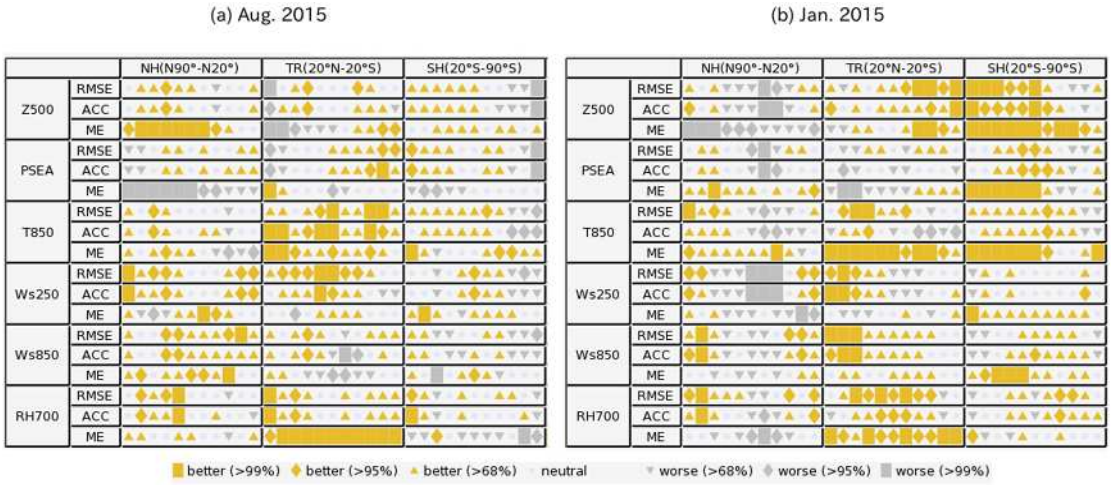

Fig. 3 Significance of improved forecast skill scores in the experiment using the GSM with the new scheme (TEST) against that with the previous scheme (CNTL). Scores represent root mean square errors (RMSEs), anomaly correlation coefficients (ACCs) and mean errors (MEs). Verification is performed for 500 hPa height (Z500), sea level pressure (PSEA), 850 hPa temperature (T850), 250 and 850 hPa wind speed (Ws250 and Ws850) and 700 hPa relative humidity (RH700), averaged over the Northern Hemisphere (NH), the tropic region (TR) and the Southern Hemisphere (SH). Yellow (gray) marks indicate better (worse) scores with statistical significance levels of 68, 95 and 99%. The 11 marks in each cell correspond to forecast days (from left (day 1) to right (day 11)). Evaluation terms are (a) August 2015 and (b) January 2015.

References

Hess, M., P. Koepke, and I. Schult, 1998: Optical properties of aerosols and clouds: The software package OPAC. *Bull. Am. Meteorol. Soc.*, **79**, 831–844.

Lau, W. K.-M., K. M. Kim, Y. C. Sud, and G. K. Walker, 2009: A GCM study of the response of the atmospheric water cycle of West Africa and the Atlantic to Saharan dust radiative forcing. *Ann. Geophys.*, **27**, 4023−4037.

Petters, M. D., and S. M. Kreidenweis, 2007: A single parameter representation of hygroscopicity growth and cloud condensation nucleus activity. *Atmos. Chem. Phys.*, **7**, 1961–1971.

WMO, 1986: A preliminary cloudless standard atmosphere for radiation computations. World Climte Programme, WCP-112, WMO/TD-No.24, 53 pp.

Yukimoto, S., H. Yoshimura, M. Hosaka, T. Sakami, H. Tsujino, M. Hirabara, T. Y. Tanaka, M. Deushi, A. Obata, H. Nakano, Y. Adachi, E. Shindo, S. Yabu, T. Ose and A. Kitoh, 2011: Meteorological Research Institute Earth System Model Version 1 (MRI-ESM1) -Model Description-. *Technical Report of the Meteorological Research Institute*, **64**, 83 pp.

Upgrade of parameterization schemes in JMA's operational global NWP model

Hitoshi Yonehara, Takayuki Tokuhiro, Ryoji Nagasawa, Masashi Ujiie, Akira Shimokobe, Masayuki Nakagawa, Ryouhei Sekiguchi, Takafumi Kanehama, Hitoshi Sato, Kei Saitou
Japan Meteorological Agency, Tokyo, Japan
(email: yonehara@met.kishou.go.jp)

1. Introduction

In March 2016, the Japan Meteorological Agency (JMA) began operation of an upgraded Global Spectral Model (GSM: JMA 2013) in which various parameterization processes (such as deep convection, cloud, radiation, land model and sea surface) were substantially revised to improve the representation of atmospheric characteristics. In this development, careful research was conducted over several interrelated physics schemes to disentangle compensating errors. As a result, several undesirable forecast characteristics that could not be eliminated via single-process refinements were excluded. This report briefly outlines the parameterization upgrades and related aims.

2. Parameterization improvement

(a) Deep convection

In the convection scheme, the artificial energy correction method used to compensate for the lack of melting process was eliminated. As this approach was artificial and ad hoc, heat and humidity tendencies were estimated unphysically and with low accuracy. It was replaced with a melting process for convective rainfall. As this change resulted in excessive heat from melting and unrealistic convective rain distribution, the sub-cloud model of the convective scheme was improved with the introduction of Kessler-type auto-conversion to reduce upward transportation of water content. Below the cloud base, a new entraining plume model based on Jakob and Siebesma (2003) was also adopted, and artificial adjustment of detrained cloud ice was stopped.

(b) Cloud

Clouds are prognostically determined in a fashion similar to that proposed by Smith (1990) with a top-hat-shaped probability distribution function whose width depends on deep convection scheme mass flux. This mass-flux dependency was eliminated to reduce grid point storms occurring as a result of the convection sub-cloud model revision. The prediction equation for cloud icefalling, which included artificial unphysical terms (Kawai 2005), was also revised. Additionally, the time discretization method was improved to reduce dependence on the time integration interval. As these changes resulted in slower cloud ice descent, the amount of high cloud increased in the mid-to-high latitudes and elsewhere. Due to easing of high cloud amount deficiency, downward long-wave radiation error near the surface was reduced.

(c) Sea surface

Surface exchange coefficients based on the Monin-Obukhov similarity theory (Beljaars and Holtslag 1991) were introduced for bulk exchange formulation of sea surface fluxes, and an improved sea ice model with more layers was adopted. Tiling between open water and sea ice was also introduced, with the approach suggested by Best et al. (2004) followed as a coupling strategy. As a result of these improvements, winter boundary layer cold biases at high latitudes were reduced via improvement of low-temperature bias in sea ice areas.

(d) Land model

In the land model, overall specifications were comprehensively updated and refined schemes were introduced. Specifically, the force-restore method for soil temperature prediction was replaced with a multilayer soil heat and water flux model and separate layers for snow. A new snow model with up to four layers was also introduced, with consideration for thermal diffusion, increased density from snow compaction and reduction of albedo due to snow aging. The distribution of vegetation types was further updated based on GLC2000. The new model provides higher levels of detail and precision, but atmospheric issues cause deterioration of boundary layer cold biases at high latitudes in winter with this improvement alone. There were a shortage of downward longwave radiation and low-temperature bias from the sea ice model in such areas. The new land model was suitable for implementation only after the improvement of other parameterization schemes.

(e) Radiation

A practical independent column approximation method for shortwave radiation cloud overlap in the cloudy area of the column was also adopted to replace random overlap (Nagasawa 2012). For a mixed state between spread anvil and narrow tower cloud (i.e., deep convection), cloud optical thickness was overestimated in shortwave radiation calculation with the previous random overlap approach. Parameterization methods for the liquid water cloud optical properties in shortwave and longwave radiation were also improved (Dobbie et al. 1999; Lindner and Li 2000).

3. Verification results

An experiment was conducted to evaluate the upgraded GSM's performance. Figure 1 shows that tropical cyclone track forecast errors for the northwestern Pacific region were reduced, and further verification indicated improvement in the new model's performance for cyclone identification. Figure 2 shows profiles of root mean square errors (RMSE) against analysis for 11-day forecasting of temperature vertical profiles. The verification region was the Northern Hemisphere (20 – 90°N), and the trial period was one month. The GSM upgrade reduced RMSE values for most pressure levels and all forecast times. Overall improvement was also seen in forecasts of other elements such as geopotential height and wind.

4. Summary

In previous GSM development, the omission of consideration for a number of major processes resulted in dramatic accuracy improvements from the enhancement of single processes. Such cases are now rare, and improvement of individual processes often exposes previously hidden issues. Accordingly, there is a need to identify the causes of issues arising and correct other processes at the same time. In the development reported here, several interrelated physics processes were intensively examined toward comprehensive improvement of GSM prediction. This strategy led to overall improvement in forecasts of geopotential height, temperature, humidity, rain, tropical cyclone track forecast error and other elements.

References

Beljaars, A. C. M. and A. A. M. Holtslag, 1991: Flux parameterization over land surfaces for atmospheric models. *J. Appl. Meteor.*, **30**, 327 – 341.

Best, M. J., A. C. M. Beljaars, J. Polcher, and P. Viterbo, 2004: A proposed structure for coupling tiled surfaces with the planetary boundary layer. *J. Hydr. Meteorol.*, **5**, 1271–1278.

Dobbie, J., J. Li, and P. Chýlek, 1999: Two- and four-stream optical properties for water clouds and solar wavelengths. *J. Geophys. Res.*, **104**, 2067–2079.

Jakob, C., and A. P. Siebesma, 2003: A new subcloud model for mass-flux convection schemes: Influence on triggering, updraft properties, and model climate. *Mon. Wea. Rev.*, **131**, 2765–2778.

Japan Meteorological Agency, 2013: Outline of the Operational Numerical Weather Prediction at JMA. Japan Meteorological Agency, Tokyo, Japan.

Kawai, H., 2005: Improvement of a Cloud Ice Fall Scheme in GCM. *CAS/JSC WGNE Res. Activ. Atmos. Oceanic Modell.*, **35**, 4.11-4.12.

Lindner, T. H., and J. Li, 2000: Parameterization of the optical properties for water clouds in the infrared. *J. Climate*, **13**, 1797–1805.

Nagasawa, R., 2012: The Problem of Cloud Overlap in the Radiation Process of JMA's Global NWP Model. *CAS/JSC WGNE Res. Activ. Atmos. Oceanic Modell.*. **42** , 4.15-4.16.

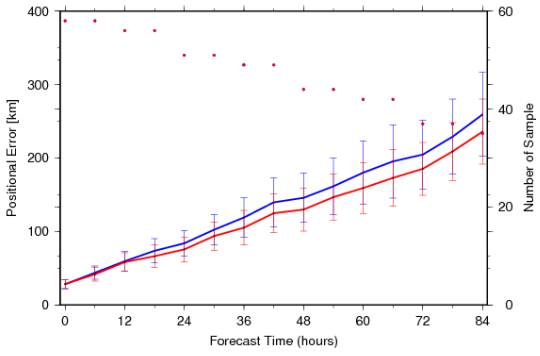

Fig. 1: Tropical cyclone track forecast errors for the northwestern Pacific region with reference to JMA best-track data. The red and blue lines show track errors for the new and old models, respectively (left axis), and each point shows the number of samples (right axis). Error bars indicate the two-sided 95% confidence interval.

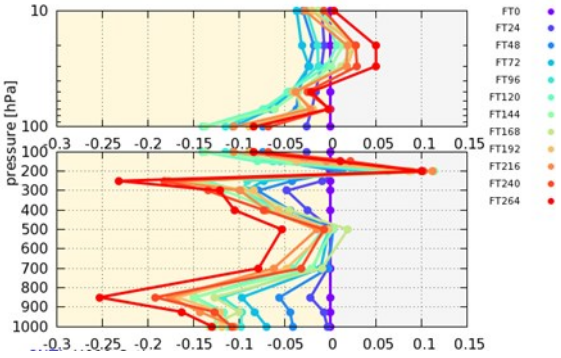

Fig. 2: Profiles of RMSE differences (new – old) for temperature [K]. The reference values are respective analysis results, and the verification region is the Northern Hemisphere (20 – 90°N). The trial period was Aug. 2015. The lines show results for a forecast time from FT = 0 h to FT = 264 h at 24-hour intervals.